

# Investigation of Ship Tracks in ATSR-2 Satellite Imagery

Hisashi Arakawa

## ABSTRACT

Aerosols in emissions from ships perturb the marine boundary layer and form regions of increased reflectance, known as ‘ship tracks’. Tracks allow us to investigate the effect of anthropogenic aerosols on Earth’s climate, which is well-known but poorly quantified. In this study, satellite data from ATSR-2 were used to investigate the properties of ship tracks. On average, the effective radius decreased from  $14.9 \mu\text{m}$  in background clouds to  $9.6 \mu\text{m}$  in ship tracks and the bright temperature decreased from 268.5 K to 264.9 K. Automated track detection algorithm was run on a larger dataset and its results were compared with those from visual analysis to test its validity. The results were used to devise ways of improving the reliability and efficiency of the algorithm.

---

## 1 Introduction

Investigation of effects that atmospheric aerosol particles have on Earth’s radiation balance is important in understanding the contribution of anthropogenic pollution to climate change. Aerosols can affect Earth’s climate in two different ways. One is the direct effect in which they scatter, absorb and reflect the incoming solar and infrared radiation. The other is the indirect effect in which they act as cloud condensation nuclei (CCN) and affect cloud radiative properties, which lead to changes in cloud albedo. Despite the significant influence of aerosols on Earth’s radiation budget, relatively little is known about how they affect the radiative forcing. This is due to their large spatial and temporal

variability, making it difficult to study their influence on clouds [1]. However, ship tracks are relatively easy to observe, providing us with interesting examples of cloud albedo modification by anthropogenic aerosols [2]. They are regions of enhanced cloud reflectance formed by aerosols in emission from ships.

The main objectives of this study were to investigate the properties of ship tracks and devise ways of improving an existing algorithm for detecting them from ATSR-2 satellite imagery. In the first part of this study, the differences in properties of ship tracks and background clouds were investigated and quantified. In the second part, the algorithm was run on several images and its results were compared with those from visual analysis for validation. In the final part, these results are discussed in the context of improving the algorithm so that it produces results compatible with those from visual analysis.



Figure 1: Ship tracks in the Pacific Ocean.

### 1.1 ATSR-2

The Along Track Scanning Radiometer 2 (ATSR-2) is an instrument on-board the ESA ERS-2 satellite, which is in a sun-synchronous orbit at a mean height of 780 km with an orbital period of about 100 minutes [9].

The along track scanning system makes observations of the same point from two

viewing geometries: the forward view, which is at an angle of  $55^\circ$  towards the direction of flight, and the nadir view, in which the radiometer views vertically downward. The radiometer is looking through different amounts of atmosphere at different angles so that the atmospheric correction can be determined by comparing measurements from the two views. The curved swath of each scan is 500 km, which corresponds to 555 pixels across for the nadir view and 371 for the forward view. The nominal instantaneous field view pixel size is  $1 \text{ km} \times 1 \text{ km}$  for the nadir view and  $1.5 \text{ km} \times 2 \text{ km}$  for the forward view.

The ATSR-2 instrument makes observations in infrared channels at 1.6, 3.7, 10.8 and  $12.0 \mu\text{m}$ , and in visible channels at 0.55, 0.67 and  $0.87 \mu\text{m}$ . The calibration of these channels is performed with an on-board visible calibration system which includes two blackbody targets.

## 1.2 GRAPE

In this study, dataset retrieved using ATSR-2 for the GRAPE (Global Retrieval of ATSR Cloud Parameters and Evaluation) project was analysed. The GRAPE project aims to produce a global dataset of cloud parameters, which can be compared with model simulations. The data is available at a lower resolution of  $3 \text{ km} \times 4 \text{ km}$ , making the analysis less computationally expensive without having much effect on the accuracy of ship track detection.

## 1.3 Ship tracks formation

### 1.3.1 Droplet growth by condensation

Water droplets can be formed through chance collisions of vapour molecules but their survival depends on whether condensation or evaporation is more efficient. The change in Gibbs free energy associated with the formation of a water droplet of radius  $a$  is given by [10]:

$$\Delta G = 4\pi a^2 \sigma - \frac{4}{3}\pi a^3 n_w k_b T \ln\left(\frac{e}{e_w}\right) \quad (1)$$

where  $a$  is the drop radius,  $\sigma$  is the surface tension,  $n_w$  is the droplet number density,  $e$  is the vapour pressure and  $e_w$  is the saturation vapour pressure over a plane surface of water at temperature  $T$ .

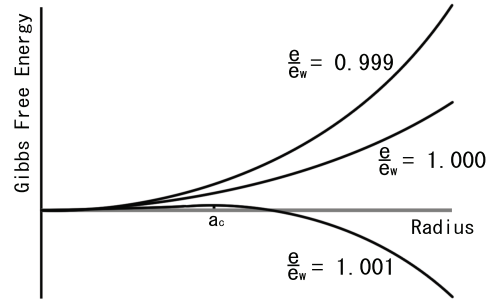


Figure 2: Change in Gibbs free energy as a function of droplet radius.

It can be seen from Figure 2 that an increase in  $a$  by condensation is more energetically preferential than evaporation if  $a > a_c$  under supersaturated conditions ( $\frac{e}{e_w} > 1$ ).

CCN support condensation by letting water spread over their surfaces. They provide ideal sites for droplet formation as they require less supersaturations for condensation to occur, and have shapes similar to those of water droplets.

### 1.3.2 Effect of ship exhaust

Aerosols contained in ship exhaust plumes can increase the concentration of CCN, which in turn lead to the formation of ship tracks in the marine boundary layer [2]. Ship plumes also contain moisture and heat but their impact on cloud formation is not as significant as aerosols [4]. The type of fuel burned by a ship plays an important role in determining

whether or not it will produce a track [3, 23].

The effect of CCN on clouds can also be deduced by considering their optical thickness. The optical thickness of a cloud of depth  $h$  containing at height  $z$  above cloud base at wavelength  $\lambda$  is given by [7]

$$\tau = \int_0^h k_E dz \quad (2)$$

where  $n(r, z)\Delta r$  drops of radius  $r \rightarrow r + \Delta r$  is the drop concentration,  $Q_E(r/\lambda)$  is the extinction efficiency and  $k_E$  is the extinction coefficient. For solar wavelengths and realistic drop distributions, this formula reduces down to

$$\tau = 2\pi N \bar{r}^2 \quad (3)$$

where  $N$  is the drop concentration and  $\bar{r}$  is the mean drop radius. The formula suggests that an increase in drop concentration leads to an increase in optical depth for a given droplet radius. An increase in the concentration of droplets result in a reduction in their sizes [12]. Since the droplet concentration is inversely proportional to volume or  $\frac{1}{r^3}$ , optical depth is proportional to  $\frac{1}{r}$ . This means that a reduction in cloud droplet size also leads to an increase in optical depth. In addition, a reduction in cloud droplet size may lead to the suppression of drizzles, which results in an increase in liquid water content. This change in liquid water content has an effect of increasing cloud albedo and a significant impact on Earth's hydrological cycle [24].

As discussed at the beginning, an increase in aerosol concentration leads to a decrease in cloud albedo due to more absorption. This has a warming effect on Earth's climate but the aforementioned cooling effects dominate in thin to moderately thick clouds. Since most of the clouds are not very thick, this suggests that pollution increases cloud albedo and has an overall cooling effect - a negative radiative forcing on Earth's climate. A study of satellite

data from MODIS showed that ship emissions, on average, reduce the solar radiation at the surface by  $2.1 \text{ Wm}^{-2}$  and increase the backscattered radiation by  $2.2 \text{ Wm}^{-2}$  [16].

It is important to note that the background and environmental conditions also play a significant role in the formation of clouds [11]. Ship tracks tend to form in regions of high humidity, small air-sea temperature differences, and moderate winds. Their occurrence drops sharply as boundary layer depth increases above about 800m. This is due to a reduction of CCN concentration and the existence of internal stable layers that prevent the mixing of aerosols [6].

## 1.4 Previous automated detection techniques

### 1.4.1 Aircraft contrail detection and segmentation

Aircraft contrails in satellite images can be detected by applying a ridge detection operator, followed by the Hough transform [14]. Detection of ridges, which are linear regions of increased reflectance, is performed by seeing if local maxima points in a  $6 \times 6$  neighbourhood connect linearly in a horizontal, vertical, or diagonal direction, in the following way:

$$\begin{array}{ccccccccc} 0 & 0 & 0 & 1 & 0 & 0 & 0 & 1 & 0 & 0 & 0 & 1 \\ 1 & 1 & 1 & 0 & 1 & 0 & 0 & 1 & 0 & 0 & 1 & 0 \\ 0 & 0 & 0 & 0 & 0 & 1 & 0 & 1 & 0 & 1 & 0 & 0 \end{array}$$

The Hough transform is then used to map a point in the  $xy$ -plane into a line in the Hough parameter space  $(m, b)$ . The parameters  $m$  and  $b$  are the slope and intercept of a line of the form  $y = mx + b$ . This way, ridges that are part of the same line are identified even if there are line breaks. The end of drop off on either side of the ridge is then identified and all the points in between are labelled as being contrail pixels.

### 1.4.2 Ship track detection

The ship track detection algorithm developed by White [15], which is used in this study, works in three steps. Firstly, suitable pixels are selected by applying filters on brightness temperature and intensity. This is to select pixels that are low enough in altitude and have intensities above a certain threshold. Ridgelets are then defined using the aforementioned method of selecting linearly connected pixels. In the last step, a set of connectivity rules are used to trace along ridgelets until it reaches an end. Ridges that satisfy a certain threshold for length are then classified as ship tracks.

### 1.4.3 Artificial neural networks

Ship track detection algorithms using the artificial neural network (ANN) have been developed in previous studies. An ANN is a system of mathematical functions which can be trained to find patterns in a given set of data. In order to train the network, the user needs to provide information on where the ship tracks are located in a given test scene. An algorithm developed by Redgate [17] obtained a high level of accuracy on test scenes, but not on scenes where the network had not been trained.

## 2 Method

### 2.1 The channel selection

The near-infrared wavelengths are more sensitive to changes in cloud reflectance due to ship tracks than the visible wavelengths [2]. The absorption of near-infrared radiation by clouds is very strong and the solar radiation does not penetrate more than about 100m. For this reason, the cloud reflectance is determined almost solely by the cloud droplet size distribution in some cases. In comparison, the cloud reflectance at visible wavelengths depends on cloud thickness and liquid water content, as well as cloud droplet size distribution. This means that the cloud reflectance is highly variable and that the effect of ship emissions do not

show up as clearly at visible wavelengths [1]. The near infrared channel ( $3.7 \mu\text{m}$ ) therefore would be the best channel to use for observing ship tracks. However, as the coverage of the satellite in this channel is limited, channel 4 ( $1.6 \mu\text{m}$ ) was used instead.

### 2.2 Ship track properties

In the first part of this study, the effects that aerosols have on microphysical properties of clouds were investigated. A program was written to plot cloud reflectance, effective radius and brightness temperature as a function of distance along and across ship tracks. The plot along a ship track effectively shows its time evolution, assuming that the ship is moving at a constant velocity, and the one across illustrates the difference in cloud properties between the track and the background. Frequency histograms and scatter plots were used to illustrate the distribution of cloud parameters in the two environments. The correlation coefficients were also determined to evaluate the relationship between various cloud parameters statistically.

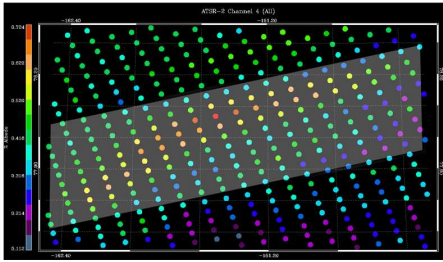
In addition, three dimensional surface plots were plotted to help visualise the time evolution of ship tracks.

### 2.3 Visual analysis

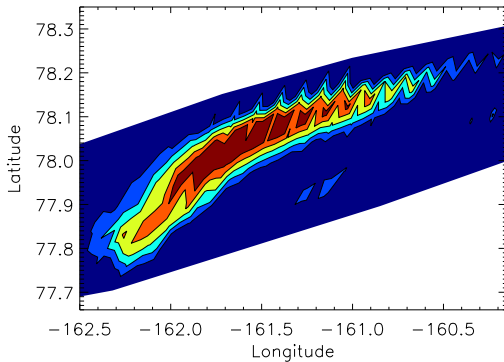
In order to test the validity of the existing automated detection algorithm, ship tracks were identified by eye and the results were compared to those obtained using the algorithm. In identifying ship tracks, a number of criteria were to be met. The first criterion is that the ship track area is more reflective than its surroundings so that it forms a ridge. The second is that it is sufficiently long and thin and has a curvilinear shape. However, those which appeared to be part of a longer ship track were counted even if they were relatively short in length. Ship tracks only form above sea so the ones over land are rejected even if they satisfy the aforementioned criteria. In

unclear cases, images were displayed in other channels for verification.

Once the ship tracks were identified, a program was written to calculate their total area. The pixel size is  $3 \text{ km} \times 4 \text{ km}$  at nadir, but it changes slightly along the swath. To take this effect into account, the program was to determine the pixel size by counting the number of data points within a specified quadrilateral and dividing it by its area. The number of data points above a certain reflectance threshold can then be counted and multiplied by the pixel size to give the total area covered by the track. The reflectance threshold was set separately for each scene as it is subject to large temporal and spatial variations.



(a) Ship tracks are selected by eye.



(b) Contour plots are shown after filtering.

Figure 3: Identification of ship tracks

When the program is run, all the pixels above the threshold are selected and inputted into an array, which is displayed on the screen as a contour plot. This allows the user to check

whether or not the appropriate threshold value has been chosen.

## 2.4 Automated detection algorithm

The satellite images are saved as HDF (Hierarchical Data Format), which is a file format used for storing scientific data such as images and arrays of vectors. An existing program called ‘loadgrapel2v2.pro’ was used to load the data structure.

Using the automated detection program called ‘trackclassify.pro’, total area of ship tracks was calculated [15]. The program works by detecting long ridges as described in the previous section.

## 2.5 The programming language

In this study, IDL (Interactive Data Language) was used to code all the programs. IDL is a programming language commonly used for analysing large data files, including images.

## 2.6 The datasets

To begin with, a satellite scene from the image taken at 19:02 (UTC) on 25 February 2000 was used for qualitative evaluation of ship track properties. This particular scene was chosen because it contains a clearly identifiable ship track which extends for over 120 km. This corresponds to a timescale of 4 hours (assuming a ship speed of  $30 \text{ kmh}^{-1}$  [21]), which is long enough for dispersion effects to be seen.

Additional satellite data became available during the project. In order to make the dataset representative of different locations at different times, images taken on 2 June, 1 July, 1 August and 1 September (all in 1997) were chosen for analysis. For each day, 4 images taken at different times were chosen, and in total 16 images were analysed.

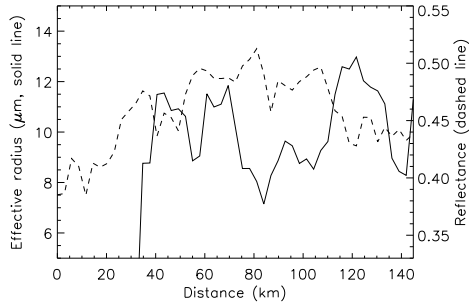


Figure 4: Effective radius and cloud reflectance as a function of distance along ship track (line A). The cut-off is due to the limited coverage for effective radius. The image was taken at 19:02 (UTC) on 25/02/00.

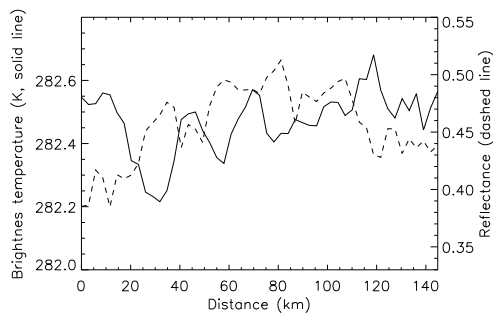


Figure 5: As in Figure 4 except for the brightness temperature.

### 3 The results

#### 3.1 Ship track properties

Figure 4 shows a significant increase in cloud reflectance (at  $\lambda=1.6 \mu\text{m}$ ) in the ship track compared to the ambient cloud. The maximum reflectance and the minimum effective radius occur at the same point, which suggests that there is a strong correlation between the two parameters.

Similar results were obtained for the brightness temperature, as shown in Figure 5. Both effective radius and brightness temperature vary greatly along the ship track.

Figure 6 and 7 show that the effective radius and brightness temperature vary substantially across the ship track. However, it can be seen that an increase in one of the parameters does

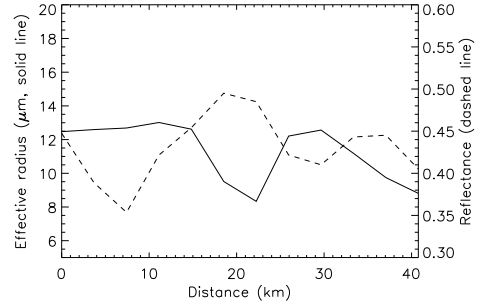


Figure 6: Effective radius and albedo as a function of distance across ship track (line B).

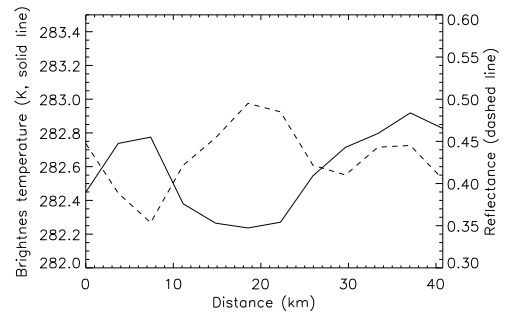


Figure 7: Brightness temperature and albedo as a function of distance across ship track (line B).

not necessarily lead to a decrease in the other. This is likely to be due to variations in other microphysical properties including the droplet concentration.

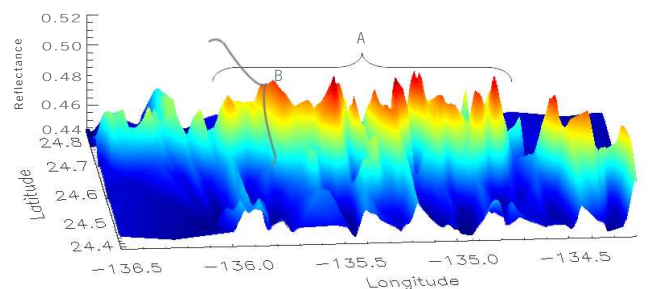


Figure 8: Surface plot of the ship track off the west coast of California.

Table 1: Average ship track and background conditions, standard deviation in parenthesis.

|                                    | Ship track    | Background    |
|------------------------------------|---------------|---------------|
| Effective radius ( $\mu\text{m}$ ) | 9.63 (6.46)   | 14.94 (9.42)  |
| Brightness temperature (K)         | 264.9 (13.0)  | 268.6 (21.6)  |
| Reflectance                        | 0.449 (0.108) | 0.328 (0.119) |

### 3.2 Statistical correlations

A single track can be highly variable in its radiative properties [1]. However, the variability tends to be averaged out when using larger datasets.

Ship tracks found in satellite images taken on 2 June 1997 at 00:01, 01:42, 05:03 and 06:43 (UTC) were analysed to see if the results from the previous subsection hold for a larger dataset and also to evaluate the statistical correlations between aerosol and cloud properties. In total, 28 ship tracks (5670 data points) were identified in the dataset.

The results of this analysis, which are presented in Table 1, show reductions in average effective radius and brightness temperature in ship tracks compared to background clouds. The reflectance is 36.9 % higher in tracks whilst the effective radius and the brightness temperature are 35.5 % and 1.4 % lower, respectively.

Figure 9 shows the statistical distribution of effective radius for tracks and background clouds. The method of applying a filter with a certain threshold reflectance value was used to select ‘cloudy’ pixels in the background [16]. The threshold values were chosen to be 0.15 - 0.17 after careful inspection of each image. It can be seen that a significant proportion of the background distribution are above 24  $\mu\text{m}$ , which corresponds to the maximum of the ship track distribution. In addition, a large proportion of tracks are in the 1 - 10  $\mu\text{m}$  range, which is not the case for background clouds. Similar observations were made for the brightness temperature at 250 K.

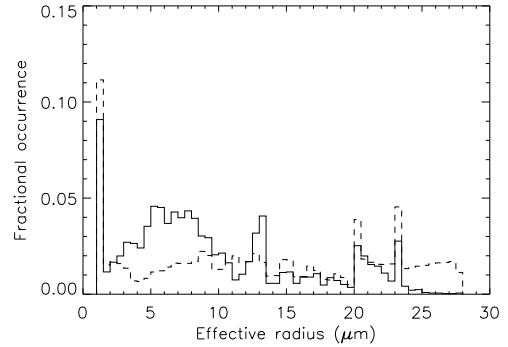


Figure 9: Histogram of the frequency of occurrence of effective radius for ship tracks, solid line, and background clouds, dashed line. Bin size is 0.5.

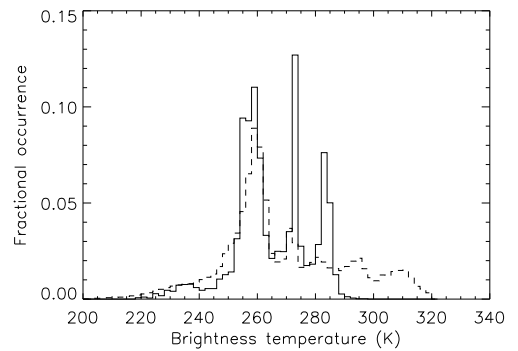


Figure 10: Same as Figure 9 except for the brightness temperature. Bin size is 2.

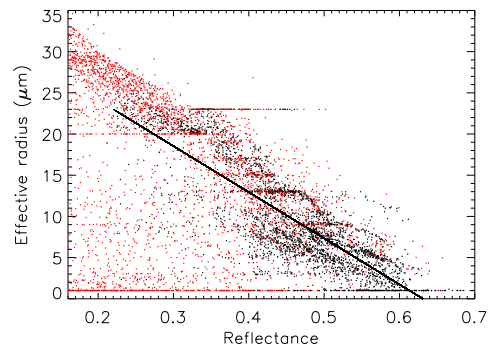


Figure 11: Effective radius plotted against reflectance within ship tracks (black) and background clouds (red). Background cloud data from the image taken at 00:01 on 02/06/97 and data for 146 ship tracks (both 3369 data points) are included.

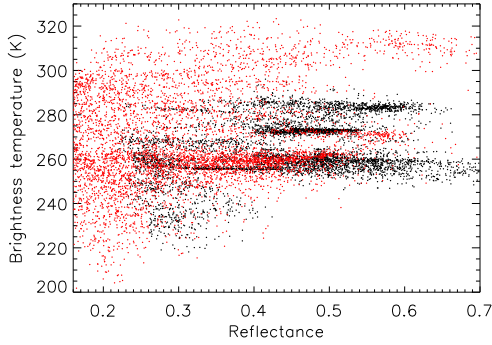


Figure 12: Same as Figure 11 but for the brightness temperature. Background cloud data from the image taken at 00:01 on 02/06/97 and data for 146 ship tracks (both 5270 data points) are included.

The relationship between effective radius and reflectance within ship tracks and background clouds was also investigated. Figure 11 shows the plot of effective radius against reflectance in tracks and background clouds. All data points in the background cloud dataset were plotted initially, but this caused the plot to be flooded. Instead, 5270 data points (size of the ship track dataset) in the background cloud dataset were chosen by systematic sampling.

The correlation coefficient between the two parameters was calculated to be -0.81, which suggests a large negative correlation in tracks. The correlation coefficient in background clouds was found to be -0.36, which also suggests a correlation but to a lesser extent. This means that a decrease in cloud effective radius with increased reflectance is more evident in ship tracks.

Figure 12 shows the brightness temperature as a function of the reflectance for ship tracks and background tracks. The relationship between effective radius and reflectance within ship tracks and background clouds was also investigated. The correlation coefficient between the two parameters was calculated to be 0.24 and 0.29 for tracks and background clouds, respectively, which shows that the

correlation is small and positive.

### 3.2.1 Further investigation on the difference in brightness temperature

The average brightness temperatures were found to be 268.5 K and 264.9 K in ship tracks and background clouds, respectively. This means that tracks appear cooler when observed in the infra-red, which is unexpected as tracks and background clouds should be at the same temperature. It may be possible that emittance is increased in ship tracks, leading to the difference in brightness temperature.

The spectral radiance  $R_\nu$  observed by the satellite is given by the radiative transfer equation [19]:

$$R_\nu = \int_0^\infty B_\nu(T(z, \infty)) \frac{\partial \mathcal{T}_\nu(z, \infty)}{\partial z} dz + \varepsilon B_\nu(T_s) \mathcal{T}_\nu(0, \infty), \quad (4)$$

where  $T(z, \infty)$  is the atmospheric temperature at  $z$ ,  $B(T)$  is the Planck function,  $T_s$  is the surface temperature,  $\mathcal{T}_\nu(z, \infty)$  is the spectral transmittance between  $z$  and the satellite, and  $\varepsilon$  is the surface emittance. For a thin cloud near the surface, the above equation can be simplified to the following:

$$R_\nu = \varepsilon B_\nu(T_c) \mathcal{T}_\nu(z, \infty), \quad (5)$$

where  $T_c$  is the cloud temperature. Assuming that ship tracks and background clouds are at the same temperature and have the same transmission values, the ratio of track to background radiances equals the ratio of emittance values for the two.

The brightness temperature is defined as the temperature of a blackbody emitting the same amount of radiation at the same wavelength. By using the Planck function, the spectral radiance of an object can be expressed as follows:

$$B_\nu(T) = \frac{2h\nu^3}{c^2 \exp[h\nu/(kT_b) - 1]} \quad (6)$$

where  $T_b$  is the brightness temperature.

Using equations (5) and (6) for a given wavelength,

$$\frac{\varepsilon_t}{\varepsilon_\phi} = \frac{\exp[hc/(\lambda k T_t) - 1]}{\exp[hc/(\lambda k T_\phi) - 1]} \quad (7)$$

where  $\varepsilon_t$  and  $\varepsilon_\phi$  is the emittance for tracks and background clouds, respectively.

For  $T_t = 264.9$  K and  $T_\phi = 268.5$  K,  $\frac{\varepsilon_t}{\varepsilon_\phi}$  equals 1.6, which suggests that the emittance is 60 % higher in ship tracks than background clouds.

### 3.3 Validation of the detection algorithm

Visual analysis was carried out on 16 images to find the total area of ship tracks in each image. In total, 146 tracks were analysed. Table 1 shows that the ship track area is highly variable, which is expected as environmental conditions can affect properties of tracks greatly [2]. In addition, tracks can last up to a day [6], which is long enough for them to be affected significantly by winds, convection and other atmospheric effects. The automated detection algorithm was run on the same dataset. Figure 13 shows that the results obtained using the algorithm (light green) are significantly higher than those from the visual analysis (navy).

Upon inspection of algorithm results, it was found that it falsely detected numerous track-like features over land. Such features can form above land for the same reason as for ship tracks, but they are due to other sources. Kaufman et al. [13] found an increase in cloud reflectance from 0.35 to 0.45 and a decrease in droplet size from 14  $\mu\text{m}$  to 9  $\mu\text{m}$  due to smoke aerosols from biomass burning in the Amazon Basin. This change is compatible with that due to aerosols in ship emissions, which explains the misidentification of track-like features over land by the algorithm.

Table 2: Summary of visual analysis results, standard deviation in parenthesis. The mean values for area ( $\text{km}^2$ ), length (km) and width (km) of ship tracks are shown.

|    | Time, Date      | Area        | Length    | Width  |
|----|-----------------|-------------|-----------|--------|
| 1  | 00:01, 02/06/97 | 1523 (1283) | 136 (71)  | 10 (4) |
| 2  | 01:42, 02/06/97 | 1867 (661)  | 137 (39)  | 13 (2) |
| 3  | 03:22, 02/06/97 | 2081 (1285) | 133 (66)  | 15 (2) |
| 4  | 05:03, 02/06/97 | 2267 (1650) | 161 (83)  | 13 (3) |
| 5  | 06:32, 01/07/97 | 842 (506)   | 83 (44)   | 10 (4) |
| 6  | 08:13, 01/07/97 | 1449 (828)  | 139 (57)  | 10 (3) |
| 7  | 09:53, 01/07/97 | 956 (565)   | 91 (40)   | 10 (4) |
| 8  | 11:34, 01/07/97 | 2027 (1596) | 165 (100) | 12 (3) |
| 9  | 06:58, 01/08/97 | 1902 (941)  | 156 (65)  | 12 (3) |
| 10 | 08:38, 01/08/97 | 1097 (745)  | 103 (56)  | 10 (3) |
| 11 | 10:19, 01/08/97 | 1325 (840)  | 105 (64)  | 12 (3) |
| 12 | 12:00, 01/08/97 | 1909 (1038) | 161 (85)  | 12 (2) |
| 13 | 07:24, 01/09/97 | 951 (395)   | 87 (42)   | 11 (1) |
| 14 | 09:04, 01/09/97 | 2325 (2009) | 195 (163) | 12 (2) |
| 15 | 10:45, 01/09/97 | 2145 (898)  | 175 (69)  | 12 (2) |
| 16 | 12:26, 01/09/97 | 1135 (722)  | 92 (39)   | 12 (3) |

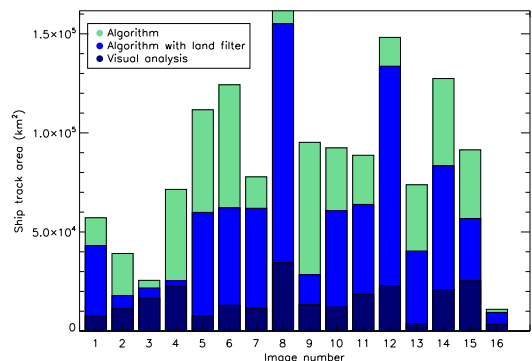


Figure 13: Histogram of total ship track area determined by detection algorithm and visual analysis. See Table 2 for details on images analysed.

Application of land-sea filter to exclude areas of land not only increased the reliability of the algorithm, but also its speed. Figure 13 shows that the difference between the algorithm (blue) and the visual analysis results decreased after the land-sea filter was applied.

In general, there were more cases of false positives (non-ship tracks being identified as ship tracks) than false negatives (real ship tracks being identified as non-ship tracks). This is discussed in more detail in the following subsection.

### 3.4 Error analysis of the algorithm

As mentioned previously, a significant proportion of ship tracks identified by the algorithm were false negatives/positives. Results obtained by the algorithm can be categorised into four groups: S-S (ship tracks being identified as ship tracks), N-S (non-ship tracks being identified as ship tracks), S-N (ship tracks being identified as non-ship tracks) and N-N (non-ship tracks not being detected).

As shown in Table 3, the desired result would be for all identified ship tracks to be in the S-S category and non-ship tracks (lack of identification) to be in the N-N category. However, most detected ship tracks were observed to fall into the N-N category. In order to quantify this result, the fractional error for S-S was determined using equation (8) for each scene.

$$\text{Fractional error} = 1 - \frac{\text{S-S}}{\text{S-S} + \text{S-N} + \text{N-S}} \quad (8)$$

Figure 14 shows the fractional error of S-S as a function of number of guesses, which is the sum of S-S, S-N and N-S for each scene. It suggests a decrease in variability of fractional error as the number of guesses increases, but only slightly. The decrease can be explained by the law of large numbers which states that the sample average converges to the population average as the number of independent samples tends to infinity. This implies that the effect of random errors can be reduced by using large sample sizes. In this case, however, it seems that there is a bias in the data, causing all values to systematically deviate by a certain amount.

Table 3: Total number of tracks detected by the algorithm categorised into four groups.

|                       | Truth  |           |
|-----------------------|--------|-----------|
|                       | Track  | Non-track |
| Detected as track     | 50 (✓) | 532 (X)   |
| Detected as non-track | 96 (X) | ✓         |

From the plot, the bias can be estimated to be about 0.89. Similarly, the biases were estimated to be 0.15 and 0.90 for N-S and S-N, respectively. By weighting the bias values by the number of samples in each category, the expected number of actual ship tracks was calculated to be 216 given that the algorithm detected 582 tracks. This is closer to the actual value of 146, but still about 50 % higher.

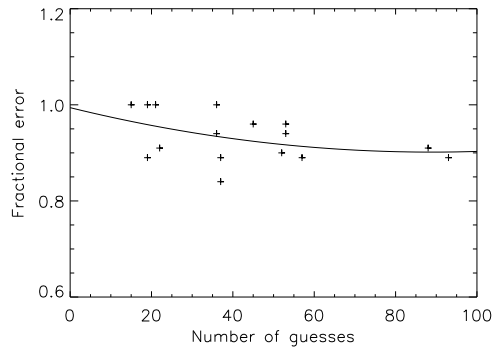


Figure 14: Fractional error of S-S plotted against number of guesses for each of the 16 scenes.

## 4 Summary and conclusions

### 4.1 Microphysical properties of ship tracks

Our analysis shows that there is an increase in reflectance and a decrease in effective radius across ship tracks, which agree with previous studies [5, 16]. On average, the effective radius decreased from  $14.9 \mu\text{m}$  in background clouds to  $9.6 \mu\text{m}$  in ship tracks, which represents a 55 % decrease. This compares well with

the decrease in effective radius from 14  $\mu\text{m}$  in the ambient cloud to 8.5  $\mu\text{m}$  in the ship track observed in the MAST experiment [20]. In addition, it was observed that there is a significant amount of fluctuations in effective radius and brightness temperature along the ship track.

Reductions in brightness temperature in ship tracks were also observed. This is an effect which has not been investigated previously, but an additional study can be conducted to test the hypothesis that the emittance is higher in tracks compared to background clouds. This may allow us to improve our understanding of the properties of ship tracks and how they are formed.

The ship tracks analysed in our analysis are, on average,  $1651 \pm 1189 \text{ km}^2$  in size,  $136 \pm 81 \text{ km}$  in length, and  $12 \pm 3 \text{ km}$  in width. The composite ship track from the MAST experiment is  $296 \pm 233 \text{ km}$  long and  $9 \pm 5 \text{ km}$  in wide [6]. The widths are in agreement with each other, but the length derived from our analysis is significantly lower. The main reason for this is that a significant proportion of tracks are truncated due to the limited swath width of 500 km.

It must be noted that the conclusions drawn from this study is dependent on the environmental conditions at the time satellite images were taken and may not be representative of ship tracks in general. In addition, the observed reflectance is also dependent on other factors such as the concentration of aerosols, which bring uncertainties into our conclusions. The effect due to random fluctuations, however, should be small as large sets of data were used to find average values.

## 4.2 Visual analysis

Even after applying the land-sea filter, there were still some discrepancies between the ship track area determined by the algorithm and the visual analysis. This is most likely due to

the algorithm picking up track-like cloud structures. A number of improvements can be made to the algorithm in order to minimise such false detection. A detailed error analysis of the algorithm follows this subsection.

## 4.3 Further development

### 4.3.1 Inclusion of effective radius checking mechanism

The results from our analysis and previous studies suggest that there is a general decrease in the effective radius across ship tracks. This result can be used as an additional criterion for track identification. Reductions in the effective radius by up to 50% have been observed in the past [8], which suggest that this is a possible criterion for distinguishing ship tracks from background clouds. However, due to the limited coverage of ATSR-2 in the effective radius channel, this method would only work for certain ship tracks.

The results given in Table 1 suggest that the brightness temperature is about 4 K in ship tracks compared to the background. This result could be used as another criterion for checking whether or not the selected area is a ship track.

### 4.3.2 Minimum and maximum widths

It was noted during the visual analysis that a number of ridges detected by the algorithm were too wide to be ship tracks. Even a small number of such misclassified tracks can change the overall result significantly as they have relatively large areas. This was in fact one of the major sources of error. An extra criterion for the track width can be added to minimise such misidentification. Given that the average track width for the dataset analysed in this study was  $12 \pm 3 \text{ km}$ , most ship tracks widths should fall within the 6-18 km ( $\bar{x} \pm 2\sigma$ ) range. However, the average width from the MAST experiment is  $9 \pm 5 \text{ km}$ , which shows that there is a large uncertainty and that it can differ considerably in different geographical locations.

### 4.3.3 Consideration of systematic error

As discussed in §3.4, systematic error can be taken into account to deduce the actual number of ship tracks from that estimated by the algorithm. However, larger datasets need to be analysed so that a more accurate value of bias can be found.

### 4.3.4 Use of information on ship routes

It was noted during the visual analysis that the densities of ship tracks are higher in certain regions, which include the west coast of California and the Sea of Japan. This can be explained by the fact that there are a number of busy trade shipping routes in these regions.

Information on ship routes can be used to check the accuracy of track detection. If ship tracks are identified in regions where no shipping routes exist, they can be discarded as false positives.

### 4.3.5 Probability density function

Figure 15 shows the distribution of ship track length obtained in our analysis. A probability density function could be built up by collecting ship track data from a larger dataset to estimate the probability of a potential ship track with a given length being a real track. This would allow us to evaluate the reliability of the automated track detection algorithm. To take into account the diurnal variation of stratocumulus clouds and other effects, data for over a year can be analysed [25].

## Acknowledgements

The author would like to thank Elies Campmany, Don Grainger and all other members of the Earth Observation Data Group for their kind support throughout the project. This project would not have been so enjoyable without them.

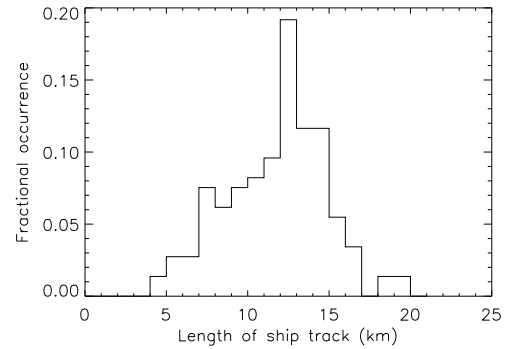


Figure 15: Probability distribution of ship track length for 146 tracks analysed in the previous section is shown by the histogram.

## References

- [1] P. A. Durkee, K. J. Noone and R. T. Bluth. The Monterey Area Ship Track Experiment. *J. Atmos. Sci.*, 57: 2523-2541, 2000.
- [2] S. Platnick, *et al.* The role of background cloud microphysics in the radiative formation of ship tracks. *J. Atmos. Sci.*, 57: 2607-2624, 2000.
- [3] P. V. Hobbs, *et al.* Emission from ships with respect to their effects on clouds. *J. Atmos. Sci.*, 57: 2570-2590, 2000.
- [4] A. S. Ackerman, *et al.* Effects of aerosols on cloud albedo: evaluation of Twomey's parameterization of cloud susceptibility using measurements of ship tracks. *J. Atmos. Sci.*, 57: 2684-2695, 2000.
- [5] M. D. King, L. F. Radke and P. V. Hobbs. Optical properties of marine stratocumulus clouds modified by ships. *J. Geophys. Res. Sci.*, 57: 2684-2695, 1993.
- [6] P. A. Durkee, *et al.* Composite ship track characteristics. *J. Atmos. Sci.*, 57: 2542-2553, 2000.
- [7] S. Twomey. The influence of pollution on the shortwave albedo of clouds. *J. Atmos. Sci.*, 34: 2684-1152, 1977.

- [8] J. P. Taylor, *et al.* Effects of aerosols on the radiative properties of clouds. *J. Atmos. Sci.*, 57: 2656-2670, 2000.
- [9] C. Mutlow, *et al.* ATSR-1/2 User Guide (Issue 1.0), 1999.
- [10] M. L. Salby. Fundamentals of Atmospheric Physics. 1996.
- [11] J. A. Coakley, *et al.* The appearance and disappearance of ship tracks on large spatial scales. *J. Atmos. Sci.*, 57: 2765-2778, 2000.
- [12] J. A. Coakley and C. D. Walsh. Limits to the aerosol indirect radiative indirect effect derived from observations of ship tracks. *J. Atmos. Sci.*, 59: 668-680, 2002.
- [13] Y. J. Kaufman, *et al.* The Effect of Smoke Particles on Clouds and Climate Forcing *Science*, 277: 1636-1639, 1997
- [14] J. M. Weiss, S. A. Christopher and R. M. Welch. Automatic contrail detection and segmentation. *IEEE Trans. Geosci. & Remote Sensing*, 35: 1609-1619, 1998.
- [15] D. White. The detection of ship tracks in ATSR2 Satellite Imagery. 2004.
- [16] M. Schreier, *et al.* Impact of ship emissions on the microphysical, optical and radiative properties of marine stratus: a case study. *Atmos. Chem. Phys.*, 6:1023-1071, 2006.
- [17] J. Redgate. The detection of ship tracks in ATSR2 Satellite Imagery. 2005.
- [18] E. Öström, K. J. Noone and R. A. Pockalny. Cloud Droplet Residual Particle Microphysics in Marine Stratocumulus Clouds Observed during the Monterey Area Ship Track Experiment. *J. Atmos. Sci.*, 57: 2671-2683, 2000.
- [19] D. G. Andrews. An Introduction to Atmospheric Physics. 2000.
- [20] P. A. Durkee, *et al.* The Impact of Ship-Produced Aerosols on the Microstructure and Albedo of Warm Marine Stratocumulus Clouds: A Test of MAST Hypotheses Ii and Iii. *J. Atmos. Sci.*, 57: 2554-2569, 2000.
- [21] J. J. Corbett, *et al.* Estimation, Validation, and Forecasts of Regional Commerce Marine Vessel Inventories., 2006.
- [22] S. J. Abel, E. J. Highwood, J. M. Haywood, and M. A. Stringer. The direct radiative effect of biomass burning aerosols over southern Africa. *Atmos. Chem. Phys.*, 5: 1999-2018, 2005
- [23] K. J. Noone, *et al.* A Case Study of Ships Forming and Not Forming Tracks in Moderately Polluted Clouds. *J. Atmos. Sci.*, 57: 2729-2747, 2000.
- [24] V. Ramanathan, P. J. Crutzen, J. T. Kiehl, and D. Rosenfeld. Aerosols, Climate, and the Hydrological Cycle. *Science*, 246: 2119-2124, 2001.
- [25] R. F. Cahalan, W. Ridgeway, W. J. Wiscombe, and T. L. Bell. The Albedo of Fractal Stratocumulus Clouds. *J. Atmos. Sci.*, 51: 2434-2455, 1994.